Article

A Human Ventricular Myocyte Model with a Refined Representation of Excitation-Contraction Coupling

Yukiko Himeno,[1] Keiichi Asakura,[1,2] Chae Young Cha,[1,3] Hiraku Memida,[1] Trevor Powell,[4] Akira Amano,[1] and Akinori Noma[1,*]

[1]Biosimulation Research Center, College of Life Sciences, Ritsumeikan University, Shiga, Japan; [2]Nippon Shinyaku Co., Ltd., Kyoto, Japan; [3]Oxford Centre for Diabetes Endocrinology and Metabolism and [4]Department of Pharmacology, University of Oxford, Oxford, UK

ABSTRACT   Cardiac Ca^{2+}-induced Ca^{2+} release (CICR) occurs by a regenerative activation of ryanodine receptors (RyRs) within each Ca^{2+}-releasing unit, triggered by the activation of L-type Ca^{2+} channels (LCCs). CICR is then terminated, most probably by depletion of Ca^{2+} in the junctional sarcoplasmic reticulum (SR). Hinch et al. previously developed a tightly coupled LCC-RyR mathematical model, known as the Hinch model, that enables simulations to deal with a variety of functional states of whole-cell populations of a Ca^{2+}-releasing unit using a personal computer. In this study, we developed a membrane excitation-contraction model of the human ventricular myocyte, which we call the human ventricular cell (HuVEC) model. This model is a hybrid of the most recent HuVEC models and the Hinch model. We modified the Hinch model to reproduce the regenerative activation and termination of CICR. In particular, we removed the inactivated RyR state and separated the single step of RyR activation by LCCs into triggering and regenerative steps. More importantly, we included the experimental measurement of a transient rise in Ca^{2+} concentrations ($[Ca^{2+}]$, 10–15 μM) during CICR in the vicinity of Ca^{2+}-releasing sites, and thereby calculated the effects of the local Ca^{2+} gradient on CICR as well as membrane excitation. This HuVEC model successfully reconstructed both membrane excitation and key properties of CICR. The time course of CICR evoked by an action potential was accounted for by autonomous changes in an instantaneous equilibrium open probability of couplons. This autonomous time course was driven by a core feedback loop including the pivotal local $[Ca^{2+}]$, influenced by a time-dependent decay in the SR Ca^{2+} content during CICR.

INTRODUCTION

Our understanding of human cardiac cell physiology has been greatly facilitated by combining limited human experimental data with mathematical myocyte models based on detailed and systematic knowledge gained by conducting animal experiments (1–3). Two of the most recent models of human ventricular cells (HuVECs), the GPB model (4) and the ORd model (5), were based on an extensive review of human data for membrane excitation, and demonstrated ionic mechanisms underlying the action potential (AP) as well as the Ca^{2+} transients at various stimulus frequencies. However, what is still required is a cell model that incorporates the updated mechanisms of Ca^{2+}-induced Ca^{2+} release (CICR), since membrane excitation is largely modified by intracellular Ca^{2+} dynamics (6). Moreover, CICR is the key mechanism in coupling membrane excitation to muscle contraction.

The empirical equations used to describe CICR so far in most cardiac cell models are of limited use because they were largely simplified. For example, the functional coupling between L-type Ca^{2+} channels (LCCs) and ryanodine receptors (RyRs) was calculated by referring to

a time-dependent increase of $[Ca^{2+}]$ in a single dyadic (or submembrane) space common to the whole population of RyRs within a cell. However, it is now well established that CICR is regulated by the tight coupling between LCCs and a cluster of RyRs individually for each Ca^{2+}-releasing unit (CaRU) (7,8) (this is known as the local control theory). Here, we define the cluster of RyRs as a couplon separate from LCCs. Moreover, the activation and inactivation kinetics of RyR models have been elucidated in much more detail by recent experimental findings.

Greenstein and Winslow (9) formulated a computational model of the cardiac ventricular myocyte that included the stochastic calculation of 12,500 individual CaRUs gating according to the local control of CICR. Subsequently, Hinch (10) and Hinch et al. (11) succeeded in reducing the computational cost of that model by developing a new algorithm (a tightly coupled LCC-RyR model, known as the Hinch model) for calculating CICR processes explicitly for each combination of open or closed conformations of LCCs and a couplon, representing a hypothetical CaRU composed of a group of RyRs. In the Hinch model, the spread of activation to neighboring CaRUs is prevented by assuming that the released Ca^{2+} is largely diluted by the bulk cytosol separating individual CaRUs, and thus the activation of RyRs is roughly proportional to the LCC activation. However, it is well established that a large Ca^{2+} gradient

occurs near the Ca^{2+}-releasing site (12–17). Any Ca^{2+} accumulation around a CaRU in general might allow the spread of sequential activation of neighbors through an increase in local $[Ca^{2+}]$ outside the CaRU.

A localized Ca^{2+} depletion within the SR has been observed during Ca^{2+} sparks by confocal imaging (18–20). The effects of this Ca^{2+} depletion were examined by theoretical calculations of the stochastic activation of individual RyRs induced by the spatiotemporal evolution of $[Ca^{2+}]$ within the dyadic cleft. It was demonstrated that the depletion of local Ca^{2+} content in the terminal cisternae of the sarcoplasmic reticulum (SR) did indeed terminate the Ca^{2+} release of CaRUs in the absence of an inactivation state of RyRs (SJ model (21), LC model (22), and SM model (23)).

The inactivation of LCC is also a pivotal element in calculating the time evolution of the state transitions of CaRUs. However, most models of Ca^{2+}-dependent inactivation (CDI) are not necessarily based on the cascade of molecular events of the CDI of LCCs (24–27). On the other hand, the Hinch model gives a Ca^{2+} concentration at the Ca^{2+}-binding site for CDI, which is consistent with the widely accepted theoretical estimation of $[Ca^{2+}]$ near the ion channel exit (25,26,28–30). If the estimation of $[Ca^{2+}]$ at the ion channel exit is realistic, the shortening of AP evoked by increasing the $[Ca^{2+}]_o$ (31,32) might be reproduced in a mathematical model through the CDI mechanism.

In our previous study (33), we used the Hinch model to examine the involvement of CICR in the development of early afterdepolarization (EAD) and delayed afterdepolarization (DAD) in a human ventricular myocyte model. Here, we decided that although the basic mechanisms of EAD and DAD would remain essentially the same, we had to improve the state transition of CaRU (11) by removing the rapid inactivation of RyR, since it has been reported that such inactivation is hardly observed in experiments (33–36). We revised the kinetics of the CICR model with respect to the Ca^{2+} dependency of the couplon closing rate, which was caused by the Ca^{2+}-dependent activation of individual RyRs that constitute the couplon. We incorporated this revised CICR model into our HuVEC model. Using this HuVEC model, we demonstrated mechanisms underlying both graded Ca^{2+} release in the presence of local Ca^{2+} accumulation, and the controlled termination of regenerative CICR in the absence of RyR inactivation. Although detailed experiments of CICR have not yet been conducted in HuVECs, it may be timely to propose a comprehensive human ventricular myocyte model that includes membrane mechanisms, mechanistic CICR models, and the contraction of myofilaments.

MATERIALS AND METHODS

Details regarding the parameters used in this work, the variables and their physical units, cell geometry, Ca^{2+} compartments, Ca^{2+} buffers, Ca^{2+} diffusion, dynamic equations for ion channels and transporters,

the CaRU, and changes in ion concentrations and membrane potential, as well as supporting figures are provided in the Supporting Material. The source code of the model can be downloaded at http://www.eheartsim.com. In this section, the Ca^{2+} compartments, the distribution of ion channels and transporters within each compartment, the definition of nanodomain (*nd*), and modifications of the Hinch model are described.

Separation of Ca^{2+} compartments in the HuVEC model

Acsai et al. (12) found a higher $[Ca^{2+}]$ transient of 10–15 μM in a near releasing site (*nrs*). According to this finding, for our HuVEC model we divided the ion diffusion space (V_{cyt}) into three Ca^{2+} compartments (a junctional space (*jnc*), an intermediate zone (*iz*), and bulk space (*blk*), as indicated with different colors in Fig. 1):

$$V_{cyt} = V_{jnc} + V_{iz} + V_{blk}. \quad (1)$$

The cytosolic Ca^{2+} gradients were represented in three discrete steps by $[Ca^{2+}]_{jnc}$, $[Ca^{2+}]_{iz}$, and $[Ca^{2+}]_{blk}$. V_{jnc} was model adjusted to 0.8% of the apparent cell volume (V_{cell}) to give an appropriate bias level for $[Ca^{2+}]$ around Ca^{2+}-binding sites within a CaRU (denoted as $[Ca^{2+}]_{nd}$). The *iz* (= 3.5% of V_{cell}) defines an intermediate zone between *jnc* and *blk*, and may correspond to *nrs* in Acsai et al. (12).

The ion channels and transporters were distributed on the sarcolemma. I_{CaL} due to LCCs composing the CaRU at *nd* were assigned to *jnc*. To simulate CDI of whole-cell I_{CaL}, we assigned 75% of the LCCs to the *jnc*, 10% to *blk*, and the rest to *iz*. Other $[Ca^{2+}]$-related currents, such as I_{Ks}, I_{Cab}, $I_{L(Ca)}$, I_{NCX} (Na^+/Ca^{2+} exchanger), and I_{PMCA}, were distributed in *iz* (10%), and the rest of the currents were in *blk* (90%). All of the other channels and transporters were located in *blk*. The above assumption for NCX distribution seemed to be adequate for reconstructing the experimental recording of I_{NCX} evoked by the Ca^{2+} transient during 10- and 30-ms step pulses (12). Transferring half of the NCX from *iz* to *jnc* hardly affected the result because the $[Ca^{2+}]_{jnc}$ transient diminished too rapidly to evoke NCX effectively (the absence of NCX in rat dyad was previously reported (37), although its exact location is still uncertain (38)). No compartments were assumed for Na^+ and K^+ because their diffusion was estimated to be rapid (39,40), and all ion channels or transporters independent of Ca^{2+} were assigned to *cyt* for the sake of simplicity.

Nanodomain Ca^{2+} in the CaRU

To derive an expression for the $[Ca^{2+}]$ sensed by the LCCs and RyRs, we used the rapid equilibrium approximation adopted by Hinch (10) and Hinch et al. (11). In this approach, the calcium in the nanodomain ($[Ca^{2+}]_{nd}$) is assumed to be in an instantaneous steady state, since the time constant for equilibrium in this region is considerably smaller than the open times of the LCCs or RyRs, so that the efflux of calcium into the adjoining sink (*jnc* in this study) is balanced by the currents through the LCCs and RyRs. Using the same approximation, we can define $[Ca^{2+}]_{nd}$ as a function of $[Ca^{2+}]$ in two Ca^{2+} sources, SRrl ($[Ca^{2+}]_{SRrl}$) and extracellular space ($[Ca^{2+}]_o$), and in the Ca^{2+} sink compartment directly connected to *nd* ($[Ca^{2+}]_{jnc} = [Ca^{2+}]_{00}$) and V_m:

$$[Ca]_{nd} = \frac{[Ca]_{00} + f_R \times [Ca]_{SRrl} + f_L \times \dfrac{\delta V \cdot e^{-\delta V}}{1 - e^{-\delta V}} \times [Ca]_o}{1 + f_R + f_L \times \dfrac{\delta V}{1 - e^{-\delta V}}},$$

$$f_R = 0.31, \quad f_L = 0.014,$$

$$(2)$$

where f_R ($= J_R/g_D$ (11) or r_{RyR}/r_{xfer} (41)) and f_L ($= J_L/g_D$ (11) or $P_{LCC}/(V_{ds} \times r_{xfer})$ (41)) indicate the conductivity ratio between influx (flux from
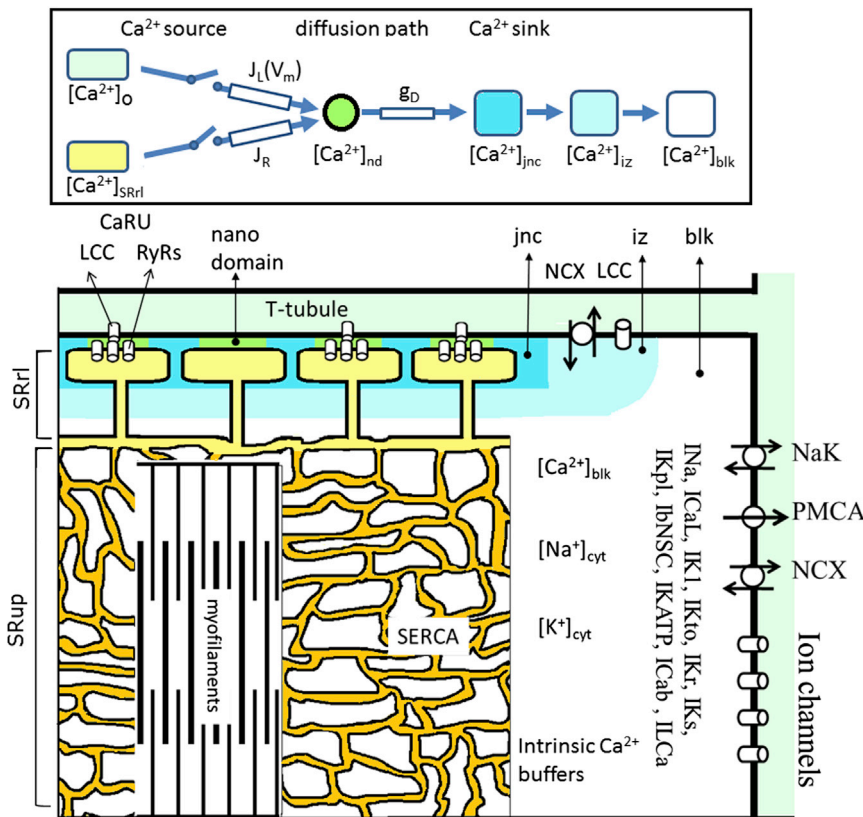
FIGURE 1 Composition of the HuVEC model demonstrated by a half-sarcomere. The compartments of *jnc*, *iz*, and *blk* in the cytosol, SR, and T-tubule are filled with different colors. The ion channels and transporters are located on the sarcolemma, SERCA and RyRs are on the SR membrane, and the contractile fibers are in *blk*. A single CaRU consists of a hypothetical LCC and a couplon in the junctional cleft (filled with *green color*), and individual CaRUs are spatially separated from their neighbors by *jnc*. The inset at the top shows a schematic presentation of the diffusion pathway of Ca^{2+} from the Ca^{2+} sources to the sink. J_L, J_R, and g_D represent the permeability of single LCCs and RyRs, and the Ca^{2+} flux rate from *nd* to *jnc*, respectively. The myofilaments were embedded in an SR network (SRup). I_{CaL}: L-type Ca^{2+} current; I_{Na}: sum of Na^+ currents in transient and late modes; $I_{NaT} + I_{NaL}$; I_{K1}: inward rectifier K^+ current; I_{Kr}: rapid component of delayed rectifier K^+ current; I_{Ks}: slow component of delayed rectifier K^+ current; I_{Kto}: transient outward K^+ current; I_{Kpl}: plateau K^+ current; $I_{I(Ca)}$: Ca^{2+}-activated background cation current; I_{Cab}: background Ca^{2+} current; I_{KATP}: ATP-sensitive K^+ current; I_{bNSC}: background nonselective cation current; NaK: Na^+/K^+ pump; NCX: Na^+/Ca^{2+} exchanger; PMCA: plasma membrane Ca^{2+} ATPase; SERCA: sarco-/endoplasmic reticulum Ca^{2+} pump.

a couplon and a hypothetical unit of several LCCs) and efflux (diffusion from *nd* to the Ca^{2+} sink compartment next to *nd*) within *nd*. δV stands for zFV_m/RT.

The first term of the numerator in Eq. 2, Ca_{00}, is the $[Ca^{2+}]$ in a functional Ca^{2+} compartment, *jnc* in the HuVEC model, which provides a direct sink of Ca^{2+} efflux from *nd* and is calculated by time integration of Ca^{2+} fluxes. The second and third terms of the numerator indicate components that are directly dependent on Ca^{2+} fluxes through a couplon or LCC, respectively. The instantaneous equilibrium of $[Ca^{2+}]_{nd}$ implies that *nd* is located on a diffusion pathway of Ca^{2+} fluxes from the source pools, i.e., the extracellular space for LCCs and the SRrl for couplons to a Ca^{2+} sink. Thus, $[Ca^{2+}]_{nd}$ takes an intermediate level between the millimolar level of $[Ca^{2+}]_o$ or $[Ca^{2+}]_{SR}$ in the source pool and the micromolar range in the sink pool. In this study, the sink pool of Ca^{2+} is defined as junctional space (*jnc*). Thus, $[Ca^{2+}]_{jnc}$ represents C_{00} in Eq. 2 and potentially is able to activate the CaRU in the absence of LCC activation, typically during a condition of Ca^{2+} overload of the SR. It should be noted that the $[Ca^{2+}]_{nd}$ has not been defined in the conventional cardiac cell models published to date, including the GPB and ORd models, but is frequently used to calculate the inactivation of LCCs in biophysical studies (26,28,30,42), as well as in the single couplon model of CICR with (43) or without (22,23) LCCs. The NL contraction model of Negroni and Lascano (44) was used without modification.

Modification of the state-transition scheme in the Hinch model

We modified the original Hinch model in three ways. First, the rapid inactivation step of RyR was removed. This was because inactivation occurred too slowly (34,35,45), and CICR termination had been reproduced in the absence of this inactivation state in the SJ, LC, and SM models. The activation and deactivation rates of a RyR were determined based on single-channel recordings obtained experimentally. Second, the state transition to activate a couplon was separated into a triggering step and the subsequent regenerative activation step of RyRs, as was previously done for the full-stochastic SJ, LC, and SM models. In these models, the triggering step by LCCs was replaced simply by randomly opening one RyR (22,23). With regard to the gating properties of LCCs, we assumed that the V_m-dependent step and the Ca^{2+}-dependent step are independent of each other, as described in Shirokov et al. (26). We determined the rate constants of LCC kinetics by using experimental data obtained from HuVECs (Fig. S2). Third, we approximated the closing kinetics of a couplon based on the coincidence of simultaneous closing of multiple RyR openings.

After the modifications described above, CaRU kinetics could be expressed by an eight-state transition scheme as shown in Fig. 2. The gating of V_m-dependent and Ca^{2+}-dependent activations of LCCs and couplon activation are indicated along the *x, y,* and *z* axes, respectively. The probability of occupying a functional state of CaRU (*Y*) is denoted as Y_{xyz}, where subscripts *x, y,* and *z* indicate open (O) or closed (C). The four kinds of $[Ca^{2+}]_{nd}$ (Ca_{00}, Ca_{L0}, Ca_{0R}, and Ca_{LR}) calculated by Eq. 2 regulate the Ca^{2+}-mediated state transition along the *y* and *z* axes. When L or R is closed, the subscript for $[Ca^{2+}]_{nd}$ becomes 0 and the corresponding value of $[Ca^{2+}]_{nd}$ is calculated by nullifying J_L or J_R, respectively, in Eq. 2. The $Y_{CCt, COt, OCt}$ or $_{OOt}$ defined by the subscript t in the functional state of Y indicates the probability of a triggered state, driven by Ca_{L0} or Ca_{00} as indicated in the scheme. Note that the regenerative step was determined by Ca_{L0} and Ca_{LR} for Y_{ooo} and by Ca_{00} and Ca_{0R} for the conformation states Y_{coo}, Y_{cco}, and Y_{oco} of CaRU.

Determination of couplon kinetics

The opening (k_{co}) and closing (k_{oc}) rate constants of RyR determined from the single RyR recordings under physiologically relevant conditions are variable in the literature (46) (Fig. S5). In this study, we adopted the rate
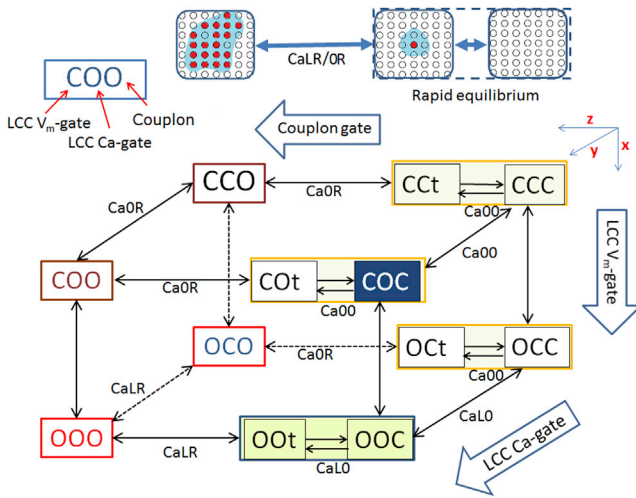
FIGURE 2 Scheme of the state transitions of the CaRU model (see text for further explanation). The inset shown at the top is a schematic illustration of a cluster of RyRs corresponding to the closed, triggered, and activated states of a couplon from right to left, respectively. Circles filled with red are open RyRs and open circles are closed ones. The blue stretch in the vicinity of open RyRs is an image of spreading Ca^{2+}. The first activation of a single RyR within a couplon is achieved either by Ca^{2+} influx through an activated LCC or by a spontaneous increase in $[Ca^{2+}]_{nd}$ during various Ca^{2+}-overload conditions.

constants used by Stern et al. (23), who referred to measurements by Guo et al. (47), to facilitate a comparison between the HuVEC model and the SM toy model. We adjusted the rates for temperature by introducing a temperature factor ($Q_{10} = 3$) after introducing a Hill equation for Ca^{2+} binding:

$$kco = Q_{10} \times \frac{0.4}{1 + \left(\frac{0.025}{[Ca]_{nd}}\right)^{2.7}} \tag{3}$$

$$koc = Q_{10} \times 0.118 \times 4.8. \tag{4}$$

The original k_{oc} (0.118 ms^{-1}) was multiplied by 4.8, referring to k_{oc} used in previous CICR models (see Fig. S5).

For the triggering step of opening a single RyR by an adjacent LCC or spontaneously, an instantaneous equilibrium was assumed, and the probability of the triggered state (f_t) of a couplon was given by

$$f_t = \frac{k_{co}}{k_{co} + k_{oc}}. \tag{5}$$

In the regenerative step, an increasing number of RyRs are activated through nearest-neighbor activation by Ca^{2+} release within a couplon, as previously demonstrated in a full-stochastic simulation by Laver et al. (22) (see their Fig. 2). For practical purposes, this mechanism was approximated by a two-state transition model between full-open and closed states of a couplon. The forward rate k_{rco} and backward rate k_{roc} of the regenerative step were determined from the single-channel RyR kinetics k_{co} and k_{oc} by Eqs. 6 and 7:

$$k_{rco} = f_n \times f_t \times k_{co} \times \left(sloc0 + [Ca^{2+}]_{SRrl}\right) \tag{6}$$

$$k_{roc} = k_{oc} \cdot pC^{(N_{RyR}-1) \cdot l} \quad where \quad pC = \frac{k_{oc}}{k_{oc} + k_{co}}. \tag{7}$$

The factor f_n in Eq. 6 is a multiplying factor (= 7 in the HuVEC model) to express the spread of Ca^{2+} to activate nearest-neighbor RyRs within a couplon in the regenerative step. The last factor of Eq. 6 is adopted from the original SM model. Equation 7 is an empirical formula deduced by conducting a stochastic simulation of open-closed-state transitions of a number ($N_{RyR} = 10$) of individual RyRs within a couplon, defining a closed event of couplon with simultaneous closure of all RyRs. The pC is a steady-state probability of the closed conformation of a RyR. The l (= 0.74) is a correcting factor for the probability of simultaneous closure of ($N_{RyR} - 1$) RyRs. Thus, k_{roc} decreases as k_{co} increases with increasing $[Ca^{2+}]_{nd}$. The lifetime of open events measured in the stochastic simulation agreed well with the k_{roc} determined by Eq. 7 at $N_{RyR} = 1$–20 or at various $[Ca^{2+}]_{nd}$. For further explanation, see "Determination of the deactivation rate of a couplon" in Supporting Materials and Methods.

The rate of change in the open probability of a couplon (pO) in a two-state transition model is then expressed as follows:

$$\frac{dpO}{dt} = k_{rco} \times (1 - pO) - k_{roc} \times pO. \tag{8}$$

We validated the overall activation and deactivation rates by performing a stochastic simulation of couplon activity (Fig. S6). Assuming the existence of 20,000 couplons in a whole cell, we observed 196 open events within 1000 ms, which is comparable to the 100 sparks/s reported for rat cardiac myocytes at a whole-cell level at rest (48).

RESULTS

Excitation and contraction in our presented HuVEC model

The new, to our knowledge, HuVEC model was able to restore a stable cycle of activity whenever the cycle length (CL) of stimulation was altered within the range examined (0.25–3 Hz; Fig. S9). A single cycle of activity is demonstrated in Fig. 3 A at a standard CL of 1000 ms. Fig. 3 A1 shows the control AP (black trace) and the AP after complete I_{Kr} block (red trace). The shape and the APD_{90} of these APs are quite comparable to those reported in Jost et al. (49) in both the control and during the I_{Kr} block: APD_{90} was prolonged from 291 to 424 ms (46% increase) as compared with 278–433 ms (56% increase) in Jost et al. (49). The standard AP parameters are comparable to those reported in ventricular myocytes (see the legend of Fig. 3 for references). The major plateau currents were I_{CaL}, I_{NaL}, and I_{NCX} in the inward direction (Fig. 3 A5), and I_{K1}, I_{Kto}, I_{Kpl}, I_{Kr}, I_{Ks}, and I_{NaK} in the outward direction (Fig. 3 A4). In Fig. 3 A2, $[Ca^{2+}]_{SRrl}$ (green) rapidly decreased from ~0.69 to a minimum level of ~0.04 mM, and $[Ca^{2+}]_{SRup}$ (chocolate) increased during the increase in $[Ca^{2+}]_{blk}$. The recovery of $[Ca^{2+}]_{SRrl}$ (green in Fig. 3 A2) was relatively slow during the AP because of the remaining small open probability of couplons due to incomplete CDI of I_{CaL}, as indicated by the plateau level of $[Ca^{2+}]_{iz}$ (~1.15 μM) at ~200–300 ms in Fig. 3 A6 (black). After repolarization, the voltage gate of LCC was totally closed by ~350 ms (black in Fig. 3 A5), and $[Ca^{2+}]_{SRrl}$ (green in Fig. 3 A2) smoothly recovered during the diastolic period as a result of the Ca^{2+} supply from SR_{up}. The peak magnitudes of the Ca^{2+} transient were 106.3, 11.1, and 0.49 μM in jnc
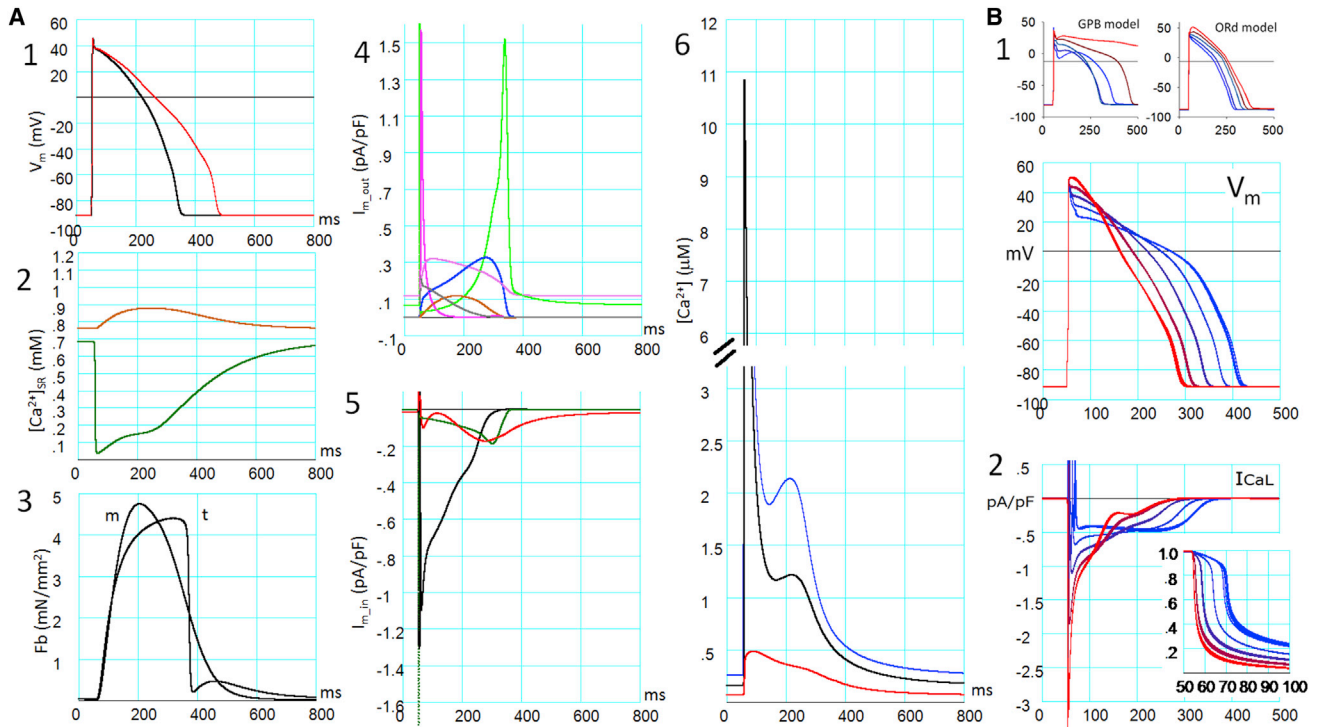
FIGURE 3 (*A* and *B*) A standard AP in the HuVEC model (*A*) and the effects of increased $[Ca^{2+}]_o$ on the AP and I_{CaL} (*B*). The AP was evoked by a 3-ms current injection at 50 ms. When stabilized at CL = 1000 ms, the AP parameters were measured. (*A1*, the resting potential) Approximately −91.4 mV (−84 mV (50), −81 mV (51), −87 mV (52)); maximum rate of rise of the AP: 244 Vs^{-1} (comparable to that in Péréon et al. (52)); duration at 90% repolarization (APD$_{90}$): 287 ms (300 ms (51,53,54); and the plateau of V_m immediately after phase 1 repolarization: ~+37.7 mV. The red AP was obtained when I_{Kr} was completely suppressed in a separate protocol. (*A2*) $[Ca^{2+}]_{SRup}$ (*chocolate*) and $[Ca^{2+}]_{SRrl}$ (*green*). (*A3*) Isotonic F_b at 6 mN/mm^2 (trace showing the delayed peak, t) and isometric F_b at 0.91 μm half sarcomere length (m) in mN/mm^2. (*A4*) Outward current components (I_{Kto} (*magenta*), I_{Kr} (*blue*), I_{Ks} (*chocolate*), I_{K1} (*yellow-green*), I_{Kpl} (*gray*), and I_{NaK} (*pink*)). (*A5*) Inward current components (I_{NaL} (*dark green*), I_{CaL} (*black*), and I_{NCX} (*red*)). The negative peak of I_{NaL} at the onset of the AP is off the scale. I_{NaT} was not plotted. (*A6*) $[Ca^{2+}]_{jnc}$ (*blue*), $[Ca^{2+}]_{iz}$ (*black*), and $[Ca^{2+}]_{blk}$ (*red*). The large transient peak of $[Ca^{2+}]_{jnc}$ is off the scale and not shown. (*B1*) APs after a change in $[Ca^{2+}]_o$ are superimposed in the GPB and ORd models (*top*). Gradient colors from blue to red are coded in reference to $[Ca^{2+}]_o$, which was increased from 0.45 to 7.2 mM by a factor of 2. The same values for $[Ca^{2+}]_o$ were applied to the HuVEC model, and five AP traces were obtained after a change in $[Ca^{2+}]_o$ are superimposed (*bottom*). (*B2*) Traces of the I_{CaL} current and open probabilities of its Ca^{2+}-dependent inactivation gate (*inset*, with an expanded timescale) are shown using the same color code as in (*B1*).

(not shown), iz (*black*), and blk (*red*), respectively (Fig. 3 *A6*). The peak of developed tension (F_b) was quite delayed in the isotonic condition (t in Fig. 3 *A3*) compared with the isometric contraction (m in Fig. 3 *A3*), and relaxed quickly after the repolarization of AP in the NL contraction model (44).

The responses of the model cell to varying stimulus frequencies over the range of 0.25–3 Hz were examined and the results agreed well with the experimental findings as well as simulation results in both GPB and ORd models (for details, see Fig. S9).

CDI of I_{CaL} revealed by varying $[Ca^{2+}]_o$

The CDI of LCCs plays a pivotal role in regulating CICR. In our previous study (33), we confirmed that CDI was retarded by preventing SR Ca^{2+} release as demonstrated experimentally (12). Here, we further examined whether our CDI model, directly influenced by $[Ca^{2+}]_{nd}$ in the Hinch formu-

lation, could reproduce the other key experimental finding that an increase in $[Ca^{2+}]_o$ shortens the duration of the AP (APD), accompanied by a positive shift of the AP plateau potential (as observed in rabbit atrial cells (32) and guinea-pig ventricular cells (55)). As a result, changes in AP obtained by varying $[Ca^{2+}]_o$ to 0.45, 0.9, 1.8, 3.6 and 7.2 mM in Fig. 3 *B1* (+37, +20, 0, −17, −35% change in APD measured at 50% repolarization, APD$_{50}$) agreed well with the experimental findings (+30, 0, −27% change in APD$_{50}$ by varying $[Ca^{2+}]_o$ to 0.62, 2.5, and 10.0 mM (32), and +45, 0, −22% change in APD$_{50}$ by varying $[Ca^{2+}]_o$ to 0.01, 1.8, 5.4 mM (55)), although the results were obtained in different animals. It was evident that CDI was accelerated with increasing $[Ca^{2+}]_o$ as shown by the open probability of the Ca^{2+}-dependent inactivation gate in Fig. 3 *B2* (*inset*). In contrast, APD was elongated with increasing $[Ca^{2+}]_o$ in the GPB and ORd models, as shown in Fig. 3 *B1*. It should be noted that previous models mostly failed to reconstruct this APD shortening with

increasing $[Ca^{2+}]_o$, except for those developed by Matsuoka et al. (56) and Grandi et al. (57), and the APD shortening effect was much smaller in those models compared with the HuVEC model. In the Hinch formulation of CaRU kinetics, the CDI of LCCs is determined by $[Ca^{2+}]_{nd}$, which is directly related to $[Ca^{2+}]_o$ when the LCC is open (Eq. 2), and this in turn increases the CDI rate ε_+ of LCCs (Eq. S5).

Initiation and termination of CICR during the AP

The state transitions of CaRU during the entire time course of an AP are shown together with V_m in Fig. 4, *A* and *B*. The transitions during the initial 15 ms of the AP are shown in Fig. 4 *C* on an expanded timescale. Just before the AP, ~99.2% of CaRUs were in Y_{coc} (*dark green*) and the rest (0.8%) were in Y_{ccc} (*lime*), indicating that the V_m gate of LCC and the couplon gate were almost completely closed. At the onset of the AP, LCC was maximally activated to Y_{ooc} (*chocolate*, step 1 in Fig. 4, *inset*). The subsequent rapid opening of couplons (steps 2 and 3) is represented by transient peaks of Y_{ooo} (*red*) and Y_{oco} (*blue*) in Fig. 4 *C*. The peak time in Y_{oco} (*blue*, step 3) was only slightly delayed because CDI of LCCs is rapid (<~1 ms). Since the V_m gate of LCC was continuously open, Y_{coo} (*magenta*) and Y_{cco} (*yellow*) scarcely appeared during the AP. The couplons closed through these rapid state transitions, and the closed conformation of couplons, Y_{occ} (*gray*), peaked at ~100 ms after the AP onset. During the subsequent repolarizing phase shown in Fig. 4, *A* and *B*, Y_{occ} (*gray*) was replaced by Y_{ccc} (*lime*) due to closure of the V_m gate of LCC (step 5). Finally, during diastole, the removal of CDI gradually proceeded to complete the recovery from Y_{ccc} (*lime*) to Y_{coc} (*dark green*) (arrow 6 in Fig. 4, *inset*).

Role of the feedback loop in determining the time courses of initiation and termination of CICR

To identify key factors in determining the activation time course of a couplon in HuVEC model, the eight-state transition scheme in Fig. 4 (*inset*) was reduced to a two-state scheme of couplon kinetics (Fig. 5, *inset A*). The overall activation and deactivation rates, $\overline{k_{rco}}$ and $\overline{k_{roc}}$, in this reduced scheme are given by a sum of the four activation rates ($k_{xyc.xyo}$) and deactivation rates ($k_{xyo.xyc}$) weighted by the probability (Y_{xyc} and Y_{xyo}) of staying in each state of the couplon:
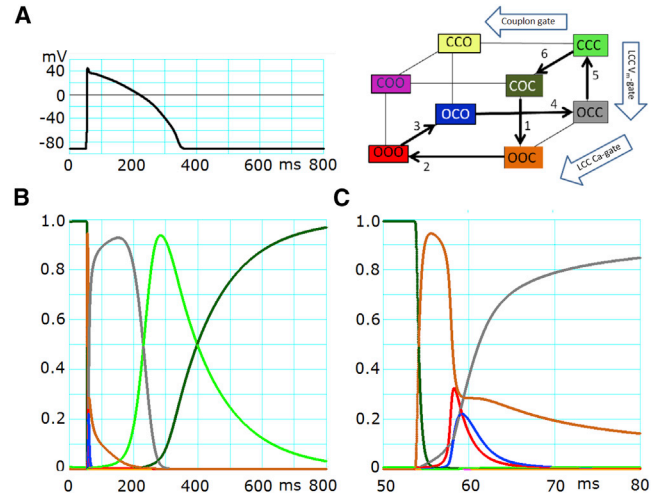

FIGURE 4 State transitions of CaRU during the AP. (*A*) The AP was triggered by a 3-ms current injection at 50 ms. (*B*) The probability of each state of CaRU is plotted on the same timescale as in (*A*) (ms). Each trace color indicates the state of CaRU of the corresponding color in the inset. Arrows 1–6 in the inset show the direction of major fluxes of the CaRU state transition after onset of the AP. (*C*) The time courses of the same state probabilities as in (*A*) are plotted on an expanded timescale for the initial period of 50–80 ms.

The rate constants $k_{xyc.xyo}$ and $k_{xyo.xyc}$ are given by Eqs. 6 and 7. The deactivation rate $\overline{k_{roc}}$ transiently decreased due to decreases in pC when $[Ca^{2+}]_{nd}$ was increased by activation of the couplon. An instantaneous equilibrium open probability of a couplon, pO_{eq}, is then calculated by the following equation, using $[Ca^{2+}]_{jnc}$, $[Ca^{2+}]_{SRrl}$, and V_m at each time step of the time integration throughout the time course of $pO(t)$:

$$pO_{eq} = \frac{\overline{k_{rco}}}{\overline{k_{rco}} + \overline{k_{roc}}}. \tag{10}$$

Fig. 5 shows the time-dependent variables involved in determining $\overline{k_{rco}}$ and $\overline{k_{roc}}$, such as V_m (Fig. 5 *A*), $[Ca^{2+}]_{SRrl}$ (Fig. 5 *B*), and the four kinds of $[Ca^{2+}]_{nd}$ (Fig. 5 *C*) on a common expanded timescale, in addition to the time course of $\overline{k_{rco}}$ and $\overline{k_{roc}}$ (Fig. 5 *D*). In Fig. 5 *E*, it is evident that $pO(t)$ (*red trace*) always follows pO_{eq} (*blue*) with a time constant τ:

$$\frac{dpO(t)}{dt} = \frac{pO_{eq} - pO(t)}{\tau} \tag{11}$$

$$\overline{k_{rco}} = \frac{k_{coc \cdot coo} \times Y_{coc} + k_{ooc \cdot ooo} \times Y_{ooc} + k_{occ \cdot oco} \times Y_{occ} + k_{ccc \cdot cco} \times Y_{ccc}}{Y_{coc} + Y_{ooc} + Y_{occ} + Y_{ccc}}$$

$$\overline{k_{roc}} = \frac{k_{coo \cdot coc} \times Y_{coo} + k_{ooo \cdot ooc} \times Y_{ooo} + k_{oco \cdot occ} \times Y_{oco} + k_{cco \cdot ccc} \times Y_{cco}}{Y_{coo} + Y_{ooo} + Y_{oco} + Y_{cco}}. \tag{9}$$
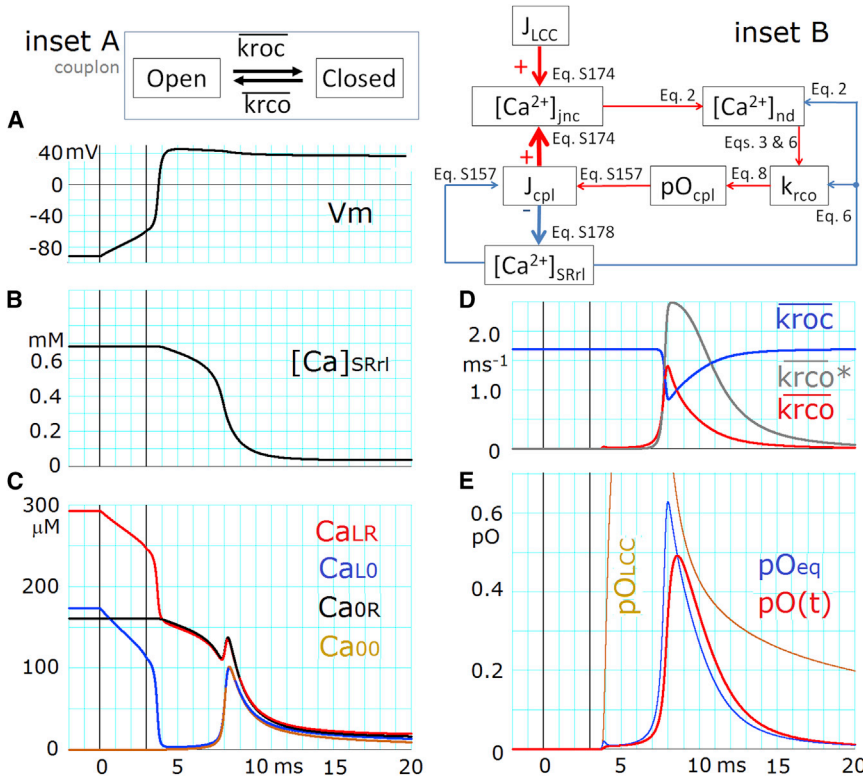
FIGURE 5 Activation and deactivation of couplons determined by the positive-feedback mechanism. (*A*) AP. (*B*) $[Ca^{2+}]_{SRrl}$. (*C*) $[Ca^{2+}]_{nd}$ (Ca$_{LR}$, Ca$_{L0}$, Ca$_{0R}$, and Ca$_{00}$). The dotted curves of CaLR, CaL0, and Ca0R indicate that they are theoretical values and have virtually no influence on the kinetics, since both the couplon and LCC are mostly closed during this period. (*D*) The overall activation rate ($\overline{k_{rco}}$) and deactivation rate ($\overline{k_{rco}}$) of the couplon and $\overline{k_{rco}}*$ were obtained after fixing $[Ca^{2+}]_{SRrl}$ to a control value. (*E*) $pO(t)$ (= $Y_{ooo} + Y_{coo} + Y_{oco} + Y_{cco}$, *red*), and pO_{eq} and pO_{LCC} ($Y_{ooo} + Y_{ooc}$; the peak is off the scale). The two vertical lines in all panels indicate the onset and offset of the stimulus current pulse. Inset A shows the reduced two-state transition of a couplon. Inset B shows the feedback loop formed by the five time-dependent variables, connected by five red arrows with equation numbers. The thick red and blue arrows indicate each Ca^{2+} release flux, which directly increases or decreases $[Ca^{2+}]_{jnc}$ or $[Ca^{2+}]_{SRrl}$, respectively.

$$\tau = \frac{1}{\overline{k_{rco}} + \overline{k_{roc}}}. \quad (12)$$

In other words, whether CICR will develop ($pO_{eq} > pO(t)$) or terminate ($pO_{eq} < pO(t)$) is decided by the movement of pO_{eq}. Fig. 5, inset B, shows the sequence of interactions among time-dependent variables involved in determining the time course of open probability of a couplon, pO_{cpl} (pO_{eq} or $pO(t)$), with corresponding equations.

At the onset of an AP, LCC is immediately and almost fully activated (pO_{LCC} in Fig. 5 E, *chocolate trace*). However, the rapid increasing phase in pO_{cpl} (Fig. 5 E, *red* or *blue*) occurred with a significant delay of ~4.5 ms after the onset of LCC activation. This delay is caused by the fact that the magnitude of I_{CaL} largely decreases when V_m shifts from the resting potential toward more positive potentials. The magnitude of Ca$_{L0}$ rapidly decreases along the AP onset (*blue trace* in Fig. 5 C, and the minimum value is 3.35 μM at ~4.5 ms), and thus Ca$_{L0}$ fails to trigger an immediate regenerative activation of the couplon. The low Ca$_{L0}$, however, activates a small but gradually increasing number of CaRUs, and thus the Ca^{2+} fluxes through couplons cause a delayed time-dependent increase in *jnc* ($[Ca^{2+}]_{jnc}$ = Ca$_{00}$, *chocolate* in Fig. 5 C). During a delay of ~4.5 ms, this Ca^{2+} accumulation progressively increases $\overline{k_{rco}}$ to generate a rapidly rising foot in pO_{cpl}. In Fig. 5, inset B, the variables connected by red arrows (pO_{cpl}, J_{cpl}, $[Ca^{2+}]_{jnc}$, $[Ca^{2+}]_{nd}$ and k_{rco}) compose a posi-

tive-feedback loop, which evokes the exponential activation of pO_{eq} and thus $pO(t)$.

On the other hand, $[Ca^{2+}]_{SRrl}$ gradually decays during 4–8 ms because of increasing Ca^{2+} release from the SR (Fig. 5 B). This decay in $[Ca^{2+}]_{SRrl}$ tends to interfere with the enhancements of $\overline{k_{rco}}$ in the positive-feedback loop, mainly by decreasing three parameters: 1) the factor ($sloc0 + [Ca^{2+}]_{SRrl}$) in Eq. 6; 2) $[Ca]_{nd}$, as indicated in Fig. 5 C (Eq. 2); and 3) J_{cpl} (J_{Ca_rel} in Eq. S157 in Supporting Materials and Methods). The net balance between the competitive effects of increasing $[Ca^{2+}]_{jnc}$ and decreasing $[Ca^{2+}]_{SRrl}$ on the positive-feedback loop is positive during the rising phase (5–8 ms) and reverses its sign in the falling phase of CICR (>9 ms).

It should be noted that these findings are entirely consistent with the results of full-stochastic simulations of CICR in a single CaRU (22,23) showing that CICR termination is driven by the feedback loop between a decrease in $[Ca^{2+}]$ in the dyadic cleft and n_{open} (in analogy to the decreasing $[Ca^{2+}]_{jnc}$ and pO_{cpl} in the HuVEC model). Indeed, the $[Ca^{2+}]_{jnc}$ (Ca$_{00}$ in Eq. 2) is a major factor in determining $[Ca^{2+}]_{nd}$ after the start of regenerative couplon activation (Fig. 5 C). The rising phase of activation of $pO(t)$ (Fig. 5 E, *red*), lasting for only a few milliseconds, is also in good agreement with that observed in the full-stochastic simulation by Laver et al. (22).

To examine the influence of the last factor in Eq. 6, the ($sloc0 + [Ca^{2+}]_{SRrl}$) was fixed to a control value (= 0.7337 mM) before stimulus onset (Fig. 5 D). The

appearance of the rising foot was slightly retarded, but the activation rate ($\overline{k_{rco}}$ *) was enlarged significantly by this intervention (*gray curve*), and the deactivation time course was prolonged, indicating that the factor ($sloc0$ + $[Ca^{2+}]_{SRrl}$) indeed decelerates activation and enhances the termination of CICR.

Graded Ca²⁺ release during voltage clamp in the ventricular cell model

In the feedback loop (Fig. 5, *inset B*), the component $[Ca^{2+}]_{jnc}$ is common to all CaRUs in the HuVEC model. Thus, Ca^{2+} accumulation in *jnc* may compromise the graded Ca^{2+} release in voltage-clamp experiments. This possibility was examined as shown in Fig. 6. Test depolarizing pulses were applied at 2 mV increments from a holding potential of −50 mV. I_{CaL} was activated in the usual voltage-dependent manner. In proportion to I_{CaL} activation, the peak amplitudes of Y_{ooo} increased (Fig. 6, *B* and *E*, graph 1). At strong depolarizations, Y_{oco} also appeared with increasing peak amplitude through CDI of LCC (Fig. 6, *B* and *E*, graph 3). In addition, Y_{coo} was activated with a markedly delayed time course of activation at negative potentials (Fig. 6 *E*, graph 4). The concomitant time evolution of Y_{coo} with Ca_{00} (= $[Ca^{2+}]_{jnc}$) (Fig. 6 *F*) indicated that this activation of Y_{coo} was largely due to the state transition from Y_{coc} to Y_{coo} evoked by the $[Ca^{2+}]_{jnc}$ accumulation.
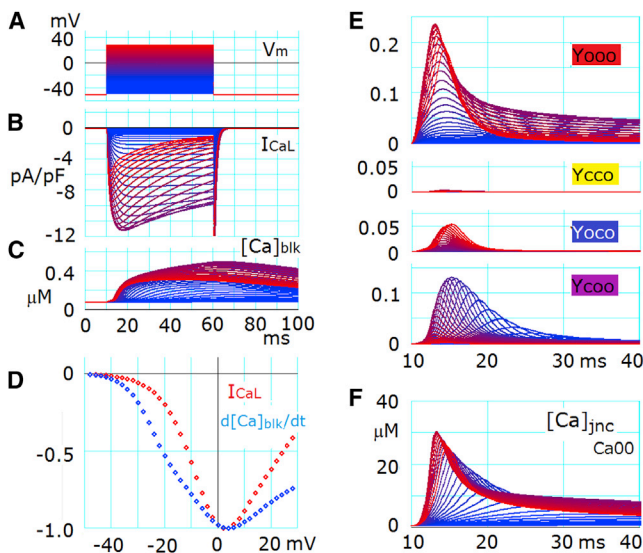
At more positive test potentials, the peak of Y_{coo} decreased because an increasing number of CaRUs were activated by the V_m-dependent LCC activation pathway as observed during the AP, i.e., the same mechanism as indicated in Fig. 4 *C* and arrows 1–4 in the inset during the AP.

To examine the influence of this CaRU activation through an increase in $[Ca^{2+}]_{jnc}$, we plotted the relationship between the test potential and the peak of $d[Ca^{2+}]_{blk}/dt$ together with the peak I_{CaL}-V_m relation after normalizing to their peaks as in a previous experimental study (7) (Fig. 6 *D*). It is evident that the HuVEC model captures key properties of the graded Ca^{2+} release even in the presence of local Ca^{2+} accumulation. The time courses of Ca^{2+} transients in *blk* evoked by each clamp pulse are superimposed in Fig. 6 *C*. One might be able to resolve the difference in the relationship between the dependencies of $d[Ca^{2+}]_{blk}/dt$ and I_{CaL} on V_m in the positive V_m range in the HuVEC model from experiment (7) by conducting voltage-clamp experiments under controlled levels of $[Ca^{2+}]_{SRrl}$.

DISCUSSION

Mathematical analysis of couplon activation

CICR in the HuVEC model is based on biophysical mechanisms to a much larger extent than that in previous human or animal cell models, which mostly used the conventional common-pool model of CICR. Here, the CICR mechanisms are compared with the models specified for CICR rather than with other whole-cell models.

The two crucial and innovative assumptions in the tightly coupled LCC-RyR kinetic model (Hinch model) remain intact in our revised model. First, the compound kinetic states of the CaRU are defined by combinations of three different gates: the V_m-dependent and Ca^{2+}-dependent gates of LCCs, and the activation gate of couplons. Second, the $[Ca^{2+}]_{nd}$ around the Ca^{2+}-binding sites for couplon activation and LCC inactivation is given by an instantaneous function of $[Ca^{2+}]$ in the two Ca^{2+} sources and the sink when the LCC and/or couplon are open (Eq. 2). To be consistent with the detailed stochastic models of CICR, however, the activation step of a couplon is separated into a triggering step and a regenerative step, which are driven by $[Ca^{2+}]_{nd}$, namely, Ca_{00} or Ca_{L0}, and Ca_{0R} or Ca_{LR}, respectively (Fig. 2). The deactivation kinetics is approximated based on the simultaneous closure of multiple RyRs within a couplon.

To reveal the mechanistic principle of CICR, we compared empirical equations among the models (see Table S6 for a comparison of explicit mathematical descriptions of the regenerative step). In the toy version of the SM model, they analytically deduced a deterministic solution of the activation rate by assembling individual reaction steps. In the SJ model, the cooperative factors CFopen and CFclose were simply defined for the regenerative activation of

FIGURE 6 Graded Ca²⁺ release evoked by voltage-clamp pulses. (*A*) Voltage-clamp pulses for 50 ms were applied from a holding potential of −50 mV to various depolarized levels, from −38 to +30 mV, in increments of 2 mV. All recordings in all panels except for (*D*) are plotted with gradient colors from blue to red, coded in reference to the test potentials shown in (*A*). (*B*) Whole-cell I_{CaL}. (*C*) $[Ca^{2+}]_{blk}$. (*D*) The voltage relationship of peak I_{CaL} (*red*) and peak $d[Ca^{2+}]_{blk}/dt$ (*blue*) was recorded with test pulses in 2 mV increments, normalized by each peak value. (*E*) Time evolution of Y_{ooo}, Y_{cco}, Y_{oco}, and Y_{coo}. (*F*) Ca²⁺ accumulation in *jnc* is represented by Ca_{00}.

RyRs and had a relatively small influence on the activation rate of a couplon (Fig. S5). In our modified Hinch model, we approximated the nearest-neighbor effect by using an activation rate (k_{rco}) that was sevenfold larger than the original single-channel rate (k_{co}) (f_n in Eq. 6), and k_{co} was accelerated with increasing $[Ca^{2+}]_{nd}$ (Eqs. 3 and 6). Thus, in all three models, the activation of a couplon was reduced to a two-state transition scheme. In both the SM and HuVEC models, the equilibrium open probability, pO_{eq}, of a couplon was examined. Stern et al. (23) disclosed an unstable equilibrium pO_{eq} (= number of open RyRs (n_{open})/number of total RyRs (n_{ry}) at a given $[Ca^{2+}]_{SRrl}$) and successfully defined a threshold pO_{eq} for both the activation and termination of couplon activity. The HuVEC model revealed that an instantaneous pO_{eq} leads to time-dependent changes in $pO(t)$, and that $[Ca]_{jnc}$ and $[Ca]_{SRrl}$ are time-dependent factors that are responsible for varying pO_{eq} (or k_{rco}) via Eqs. 3, 6, and 10. Thus, the core feedback loop (Fig. 5, inset B) is fully consistent with the view that the initiation and termination of CICR is determined by mechanisms analogous to those suggested in recent stochastic models. In the future, investigators should analyze quantitative aspects of the threshold phenomenon systematically using mathematical approaches, such as bifurcation or phase-plane analyses, to gain deeper insights into the biophysical mechanisms that underlie excitation-contraction coupling in the HuVEC model.

Verification of assuming *jnc* and *iz*

In the HuVEC model, incorporation of *jnc* and *iz* into the CICR model was a prerequisite to represent the exponential Ca^{2+} gradient by discrete $[Ca^{2+}]$ steps around the Ca^{2+}-releasing site during CICR. However, such a Ca^{2+} gradient near $[Ca^{2+}]_{nd}$ or $[Ca^{2+}]_{ds}$ was not included in the original Hinch model ($Ca_{00} = [Ca^{2+}]_{cyt}$ in Eq. 2), and Ca_{L0} was much lower than in the HuVEC model. Therefore, an activation rate constant larger than the experimental rate by more than two to three orders of magnitude was used (22,47) (see Fig. S5). This difficulty is overcome by the high $[Ca^{2+}]_{nd}$ biased by the local Ca_{00} (= $[Ca^{2+}]_{jnc}$) in the HuVEC model. Furthermore, we found that the Ca_{L0} was still too low to evoke an immediate activation of couplons by I_{CaL} (Fig. 5 C), even when we used the sevenfold larger rate constant. This is because of the sharp V_m-dependent decrease of Ca_{L0} at the AP plateau potential (Eq. 2). It turned out that the $[Ca^{2+}]_{jnc}$ in the very limited volume of *jnc* was progressively increased even by the infrequent openings of couplons to generate the foot of rapid activation of couplons through the positive-feedback loop (Fig. 5, inset B).

The presence of *jnc* was a key factor in reproducing the experimental APD shortening with increasing $[Ca^{2+}]_o$. Fig. 3 B reveals enhanced CDI of LCC with increasing $[Ca^{2+}]_o$ underlying the APD shortening. Indeed, ~90% of

CDI occurred within the initial 50 ms, during which time the peak $[Ca^{2+}]_{jnc}$ was higher by ~9-fold than the peak $[Ca^{2+}]_{iz}$, which may be comparable to $[Ca^{2+}]$ in the subsarcolemmal spaces of the GPB or ORd models. The presence of *jnc* was also essential in evoking DAD in the HuVEC model, as has been demonstrated elsewhere (33).

In a previous study, Wier et al. (7) made the interesting finding that although a brief I_{CaL} tail current observed on repolarization from +80 mV to the holding potential (−40 mV) subsided within ~2 ms, the decay of the Ca^{2+} transient due to J_{cpl} continued with a halftime of ~9 ms at the holding potential. In our HuVEC model, this delayed closure of couplons after a brief I_{CaL} tail ($t_{1/2}$ = 0.9 ms, the time to reach half of the maximum amplitude from the off time of the test pulse) was well simulated by the rate of $[Ca^{2+}]_{jnc}$ decay ($t_{1/2}$ = 4.4 ms), which was attributed to the delayed diffusion of the accumulated Ca^{2+} from *jnc* to *iz* and *blk*. Since no space was assumed for Ca^{2+} accumulation in the original Hinch model, the Ca^{2+} transient evoked by RyR activation should closely follow the time course of the I_{CaL} tail with a maximum delay of ~1 ms, as determined by k_{oc} of RyR.

Taken together, the above findings justify the incorporation of *jnc* into the HuVEC model.

Ca^{2+} compartments: *jnc*, *iz*, SR$_{rl}$, and SR$_{up}$

The $[Ca^{2+}]_{nrs}$ measured by Acsai et al. (12) was assigned to a functional space rather than a histologically defined one (58). When this large Ca^{2+} gradient was introduced into the HuVEC model, *nrs* was further divided into two hypothetical spaces, *iz* and *jnc*, and $[Ca^{2+}]_{jnc}$ was used to represent Ca_{00} in the Hinch formalism of $[Ca^{2+}]_{nd}$ (Eq. 2). Then, the volume of *jnc* was adjusted to reconstruct the key experimental and simulation results described above. Since the time course of CICR is largely determined by the size of *jnc*, V_{jnc} is compared with the volume of dyadic space (V_{ds}), which is also critical for CICR kinetics in the stochastic simulations of a single CaRU. As shown in Table 1, the V_{jnc} in our model is apparently larger than the V_{ds} assumed in other CICR models, but the difference is relatively small compared with the upper limit of V_{ds} in the LC model. Considering the effects of fixed buffer sites on membrane phospholipids or the Debye layer, the Ca^{2+} distribution volume of *ds* may increase dramatically, as indicated in Stern et al. (23). The effective size of the compartment depends on various factors, such as the kinetics of the buffers (dissociation constants), the number of available binding sites, and the membrane surface area that encloses this compartment, but not on the myoplasmic volume that it encloses (58). Therefore, it is always important to evaluate the functional volume of each compartment comprehensively.

Since $[Ca^{2+}]_{SRrl}$ is one of central factors in driving the controlled termination of CICR (Fig. 5, inset B), we also compared V_{SRrl} among different models together with

TABLE 1   Comparison of the Volumes of Junctional Ca^{2+} Compartments and [CSQN]$_{SRrl}$ among the Models

	SJ Model	LC Model	SM Model	HuVEC Model
V_{ds} or V_{jnc} in the HuVEC model	0.002–0.005[a] pL/cell 1.0×10^{-7} pL for each d.s.	0.0486–0.1215[a] pL/cell 2.43×10^{-6} pL for each d.s.	0.013–0.033[a] pL/cell cleft height 30 nm, $(7 \times 30)^2$ nm^2 area for each d.s.	0.303 pL/cell 0.8% V_{cell}
V_{SRrl}	0.2–0.5[a] pL/cell 1.0×10^{-5} pL for each CaRU	0.08–0.21[a] pL/cell 4.21×10^{-6} pL for each CaRU	0.14 pL/cell 0.35% V_{cell} assumed in the HuVEC model	0.46 pL/cell 1.2% V_{cell}
[CSQN]$_{SRrl}$	10.0 mM	30.0 mM	30.0 mM	3 mM
V_{SRup}	infinite	3.5% V_{cell}	3.5% V_{cell}	4.8% V_{cell}

In the Hinch model, 50,000 CaRUs/cell and 2×10^{-7} pL/d.s. were assumed.
[a]Calculated by assuming 20,000–50,000 CaRUs/cell.

[CSQN]$_{SRrl}$ (Table 1). Although V_{SRrl} in the HuVEC model is ~4-fold larger than the corresponding size of junctional SR in the SM model, it may be concluded that the Ca^{2+}-releasing potency of the SR-releasing site is similar between the two, because 10-fold smaller Ca^{2+} buffering power is assumed in the HuVEC model compared with the SM model. Indeed, if the number of CaRUs within a cell is assumed to be 50,000 as in the Hinch model, V_{SRrl} values in the SJ and LC models are within the same range as in the HuVEC model when a larger [CSQN]$_{SRrl}$ in each model is taken into account.

The extent of Ca^{2+} depletion in SRrl depends not only on V_{SRrl} but also on the kinetics of V_{SRrl} refilling and couplon gating. The time constant for the refilling of V_{SRrl} in the HuVEC model is ~200 ms, which is in agreement with that previously reported for rabbit (59). It should be noted, however, that the refilling time course and Ca^{2+} mobility in the SR varies between different studies (59,60). The recovery time course of local Ca^{2+} depletion, the so-called blink, is also variable between different studies (61,62). Furthermore, the separation of the SR volume into V_{SRrl} and V_{SRup} is still largely conventional and has not been explicitly determined based on experimental findings.

Limitations of the CICR model presented here

The HuVEC model successfully reproduced both electrical activity and Ca^{2+} dynamics, which were very similar to those observed in intact cells. However, the mathematical mechanisms developed in this model cell may not necessarily be a unique solution for intact cells. One limitation of the model is due to the large variety in the gating kinetics of RyRs (Fig. S5). Furthermore, if the functional size of SR Ca^{2+} compartments near the Ca^{2+}-releasing site can be established experimentally, the model will be greatly improved and enhance our understanding of the effects of local SR Ca^{2+} depletion. To test the possibility that local SR Ca^{2+} depletion, which is responsible for terminating individual couplon open events, is engaged in terminating CICR at a whole-cell level, we formulated a dyadic model with a blink space (bs) in addition to the Hinch formalism (see Supporting Materials and Methods for a theoretical treatment of bs). Our preliminary simulation using this

dyadic model with bs suggested that the general behavior of the model was essentially the same in electrically stimulated activity and voltage-clamp experiments.

Under pathophysiological conditions, Ca^{2+} waves spontaneously occur and propagate in myocytes. This Ca^{2+} wave cannot be reproduced in our HuVEC model because it has a single space of jnc and SRrl. Furthermore, in a previous study, Matsuda et al. (63) suggested that asynchronous CICR occurs spontaneously in multiple domains of the SR network within a single cell (for a simulation, see Chen et al. (64)). In that study, Matsuda et al. found that micro fluctuations remained in the recordings of the resting potential after several cyclic DAD events subsided, and suggested multiple origins of the spontaneous Ca^{2+} release with variable intrinsic rhythms under the condition of Ca^{2+} overload. Nonetheless, the assumption of common [Ca^{2+}]$_{jnc}$ and [Ca^{2+}]$_{SRrl}$ might be relevant in our simulations as long as the activation of all of the CaRUs within the cell are synchronized by an AP or a voltage-clamp pulse. To refine the CICR model, it may be necessary to conduct voltage-clamp experiments under controlled levels of [Ca^{2+}]$_{SRrl}$ (58).

SUPPORTING MATERIAL

Supporting Materials and Methods, Supporting Results, nine figures, and six tables are available at http://www.biophysj.org/biophysj/supplemental/S0006-3495(15)00599-8.

AUTHOR CONTRIBUTIONS

A.N. designed the study. A.N., K.A., C.Y.C., H.M., and Y.H. performed research and developed the HuVEC model. A.N., Y.H., A.A., and K.A. analyzed the model and wrote the manuscript with T.P.

SUPPORTING CITATIONS

References (65–90) appear in the Supporting Material.

REFERENCES

1. Priebe, L., and D. J. Beuckelmann. 1998. Simulation study of cellular electric properties in heart failure. *Circ. Res.* 82:1206–1223.

2. Ten Tusscher, K. H., O. Bernus, …, A. V. Panfilov. 2006. Comparison of electrophysiological models for human ventricular cells and tissues. *Prog. Biophys. Mol. Biol.* 90:326–345.

3. ten Tusscher, K. H., D. Noble, …, A. V. Panfilov. 2004. A model for human ventricular tissue. *Am. J. Physiol. Heart Circ. Physiol.* 286:H1573–H1589.

4. Grandi, E., F. S. Pasqualini, and D. M. Bers. 2010. A novel computational model of the human ventricular action potential and Ca transient. *J. Mol. Cell. Cardiol.* 48:112–121.

5. O'Hara, T., L. Virág, …, Y. Rudy. 2011. Simulation of the undiseased human cardiac ventricular action potential: model formulation and experimental validation. *PLOS Comput. Biol.* 7:e1002061.

6. Volders, P. G., A. Kulcśar, …, B. Szabo. 1997. Similarities between early and delayed afterdepolarizations induced by isoproterenol in canine ventricular myocytes. *Cardiovasc. Res.* 34:348–359.

7. Wier, W. G., T. M. Egan, …, C. W. Balke. 1994. Local control of excitation-contraction coupling in rat heart cells. *J. Physiol.* 474:463–471.

8. Stern, M. D. 1992. Theory of excitation-contraction coupling in cardiac muscle. *Biophys. J.* 63:497–517.

9. Greenstein, J. L., and R. L. Winslow. 2002. An integrative model of the cardiac ventricular myocyte incorporating local control of Ca2+ release. *Biophys. J.* 83:2918–2945.

10. Hinch, R. 2004. A mathematical analysis of the generation and termination of calcium sparks. *Biophys. J.* 86:1293–1307.

11. Hinch, R., J. L. Greenstein, …, R. L. Winslow. 2004. A simplified local control model of calcium-induced calcium release in cardiac ventricular myocytes. *Biophys. J.* 87:3723–3736.

12. Acsai, K., G. Antoons, …, K. R. Sipido. 2011. Microdomain [Ca^{2+}] near ryanodine receptors as reported by L-type Ca^{2+} and Na$^+$/Ca^{2+} exchange currents. *J. Physiol.* 589:2569–2583.

13. Adachi-Akahane, S., L. Cleemann, and M. Morad. 1996. Cross-signaling between L-type Ca2+ channels and ryanodine receptors in rat ventricular myocytes. *J. Gen. Physiol.* 108:435–454.

14. Sipido, K. R., G. Callewaert, and E. Carmeliet. 1995. Inhibition and rapid recovery of Ca2+ current during Ca2+ release from sarco-plasmic reticulum in guinea pig ventricular myocytes. *Circ. Res.* 76:102–109.

15. Trafford, A. W., M. E. Díaz, …, D. A. Eisner. 1995. Comparison of subsarcolemmal and bulk calcium concentration during spontaneous calcium release in rat ventricular myocytes. *J. Physiol.* 488:577–586.

16. Weber, C. R., K. S. Ginsburg, and D. M. Bers. 2003. Cardiac submembrane [Na+] transients sensed by Na+-Ca2+ exchange current. *Circ. Res.* 92:950–952.

17. Weber, C. R., V. Piacentino, 3rd, …, D. M. Bers. 2002. Na(+)-Ca(2+) exchange current and submembrane [Ca(2+)] during the cardiac action potential. *Circ. Res.* 90:182–189.

18. Cannell, M. B., and C. H. Kong. 2012. Local control in cardiac E-C coupling. *J. Mol. Cell. Cardiol.* 52:298–303.

19. Stern, M. D., and H. Cheng. 2004. Putting out the fire: what terminates calcium-induced calcium release in cardiac muscle? *Cell Calcium.* 35:591–601.

20. Zalk, R., S. E. Lehnart, and A. R. Marks. 2007. Modulation of the ryanodine receptor and intracellular calcium. *Annu. Rev. Biochem.* 76:367–385.

21. Sobie, E. A., K. W. Dilly, …, M. S. Jafri. 2002. Termination of cardiac Ca(2+) sparks: an investigative mathematical model of calcium-induced calcium release. *Biophys. J.* 83:59–78.

22. Laver, D. R., C. H. Kong, …, M. B. Cannell. 2013. Termination of calcium-induced calcium release by induction decay: an emergent property of stochastic channel gating and molecular scale architecture. *J. Mol. Cell. Cardiol.* 54:98–100.

23. Stern, M. D., E. Ríos, and V. A. Maltsev. 2013. Life and death of a cardiac calcium spark. *J. Gen. Physiol.* 142:257–274.

24. Brunet, S., T. Scheuer, and W. A. Catterall. 2009. Cooperative regulation of Ca(v)1.2 channels by intracellular Mg(2+), the proximal C-terminal EF-hand, and the distal C-terminal domain. *J. Gen. Physiol.* 134:81–94.

25. Ferreira, G., J. Yi, …, R. Shirokov. 1997. Ion-dependent inactivation of barium current through L-type calcium channels. *J. Gen. Physiol.* 109:449–461.

26. Shirokov, R., R. Levis, …, E. Ríos. 1993. Ca(2+)-dependent inactivation of cardiac L-type Ca2+ channels does not affect their voltage sensor. *J. Gen. Physiol.* 102:1005–1030.

27. Yue, D. T., and E. Marban. 1990. Permeation in the dihydropyridine-sensitive calcium channel. Multi-ion occupancy but no anomalous mole-fraction effect between Ba2+ and Ca2+. *J. Gen. Physiol.* 95:911–939.

28. Neher, E., and W. Almers. 1986. Fast calcium transients in rat peritoneal mast cells are not sufficient to trigger exocytosis. *EMBO J.* 5:51–53.

29. Stern, M. D. 1992. Buffering of calcium in the vicinity of a channel pore. *Cell Calcium.* 13:183–192.

30. Tadross, M. R., R. W. Tsien, and D. T. Yue. 2013. Ca2+ channel nanodomains boost local Ca2+ amplitude. *Proc. Natl. Acad. Sci. USA.* 110:15794–15799.

31. Kokubun, S., M. Nishimura, A. Noma, and H. Irisawa. 1982. Membrane currents in the rabbit atrioventricular node cell. *Pflugers Arch.* 393:15–22.

32. Seifen, E., H. Schaer, and J. M. Marshall. 1964. Effect of calcium on the membrane potentials of single pacemaker fibres and atrial fibres in isolated rabbits atria. *Nature.* 202:1223–1224.

33. Asakura, K., C. Y. Cha, …, A. Noma. 2014. EAD and DAD mechanisms analyzed by developing a new human ventricular cell model. *Prog. Biophys. Mol. Biol.* 116:11–24.

34. Valdivia, H. H., J. H. Kaplan, …, W. J. Lederer. 1995. Rapid adaptation of cardiac ryanodine receptors: modulation by Mg2+ and phosphorylation. *Science.* 267:1997–2000.

35. Fill, M., A. Zahradníková, …, S. Györke. 2000. Ryanodine receptor adaptation. *J. Gen. Physiol.* 116:873–882.

36. Näbauer, M., and M. Morad. 1990. Ca2(+)-induced Ca2+ release as examined by photolysis of caged Ca2+ in single ventricular myocytes. *Am. J. Physiol.* 258:C189–C193.

37. Scriven, D. R., P. Dan, and E. D. Moore. 2000. Distribution of proteins implicated in excitation-contraction coupling in rat ventricular myocytes. *Biophys. J.* 79:2682–2691.

38. Scriven, D. R., and E. D. Moore. 2013. Ca^{2+} channel and Na$^+$/Ca^{2+} exchange localization in cardiac myocytes. *J. Mol. Cell. Cardiol.* 58:22–31.

39. Hille, B. 2001. Ion Channels of Excitable Membranes. Sinauer Associates, Sunderland, MA.

40. Swietach, P., K. W. Spitzer, and R. D. Vaughan-Jones. 2015. Na$^+$ ions as spatial intracellular messengers for co-ordinating Ca^{2+} signals during pH heterogeneity in cardiomyocytes. *Cardiovasc. Res.* 105:171–181.

41. Greenstein, J. L., R. Hinch, and R. L. Winslow. 2006. Mechanisms of excitation-contraction coupling in an integrative model of the cardiac ventricular myocyte. *Biophys. J.* 90:77–91.

42. Peterson, B. Z., J. S. Lee, …, D. T. Yue. 2000. Critical determinants of Ca(2+)-dependent inactivation within an EF-hand motif of L-type Ca(2+) channels. *Biophys. J.* 78:1906–1920.

43. Williams, G. S., M. A. Huertas, …, G. D. Smith. 2007. A probability density approach to modeling local control of calcium-induced calcium release in cardiac myocytes. *Biophys. J.* 92:2311–2328.

44. Negroni, J. A., and E. C. Lascano. 2008. Simulation of steady state and transient cardiac muscle response experiments with a Huxley-based contraction model. *J. Mol. Cell. Cardiol.* 45:300–312.

45. Györke, S., and M. Fill. 1993. Ryanodine receptor adaptation: control mechanism of Ca(2+)-induced Ca2+ release in heart. *Science.* 260:807–809.

46. Qin, J., G. Valle, …, M. Fill. 2009. Ryanodine receptor luminal Ca2+ regulation: swapping calsequestrin and channel isoforms. *Biophys. J.* 97:1961–1970.

47. Guo, T., D. Gillespie, and M. Fill. 2012. Ryanodine receptor current amplitude controls Ca2+ sparks in cardiac muscle. *Circ. Res.* 111:28–36.

48. Cheng, H., W. J. Lederer, and M. B. Cannell. 1993. Calcium sparks: elementary events underlying excitation-contraction coupling in heart muscle. *Science.* 262:740–744.

49. Jost, N., L. Virág, …, S. Nattel. 2013. Ionic mechanisms limiting cardiac repolarization reserve in humans compared to dogs. *J. Physiol.* 591:4189–4206.

50. Peeters, G. A., M. C. Sanguinetti, …, W. H. Barry. 1995. Method for isolation of human ventricular myocytes from single endocardial and epicardial biopsies. *Am. J. Physiol.* 268:H1757–H1764.

51. Li, G. R., J. Feng, …, M. Carrier. 1998. Transmural heterogeneity of action potentials and Ito1 in myocytes isolated from the human right ventricle. *Am. J. Physiol.* 275:H369–H377.

52. Péréon, Y., S. Demolombe, …, D. Escande. 2000. Differential expression of KvLQT1 isoforms across the human ventricular wall. *Am. J. Physiol. Heart Circ. Physiol.* 278:H1908–H1915.

53. Li, G. R., J. Feng, …, S. Nattel. 1996. Evidence for two components of delayed rectifier K+ current in human ventricular myocytes. *Circ. Res.* 78:689–696.

54. Drouin, E., F. Charpentier, …, H. Le Marec. 1995. Electrophysiologic characteristics of cells spanning the left ventricular wall of human heart: evidence for presence of M cells. *J. Am. Coll. Cardiol.* 26: 185–192.

55. Kokubun, S., and H. Irisawa. 1984. Effects of various intracellular Ca ion concentrations on the calcium current of guinea-pig single ventricular cells. *Jpn. J. Physiol.* 34:599–611.

56. Matsuoka, S., N. Sarai, …, A. Noma. 2003. Role of individual ionic current systems in ventricular cells hypothesized by a model study. *Jpn. J. Physiol.* 53:105–123.

57. Grandi, E., F. S. Pasqualini, …, S. Severi. 2009. Theoretical investigation of action potential duration dependence on extracellular Ca2+ in human cardiomyocytes. *J. Mol. Cell. Cardiol.* 46:332–342.

58. Livshitz, L., K. Acsai, …, Y. Rudy. 2012. Data-based theoretical identification of subcellular calcium compartments and estimation of calcium dynamics in cardiac myocytes. *J. Physiol.* 590:4423–4446.

59. Picht, E., A. V. Zima, …, D. M. Bers. 2011. Dynamic calcium movement inside cardiac sarcoplasmic reticulum during release. *Circ. Res.* 108:847–856.

60. Swietach, P., K. W. Spitzer, and R. D. Vaughan-Jones. 2008. Ca2+-mobility in the sarcoplasmic reticulum of ventricular myocytes is low. *Biophys. J.* 95:1412–1427.

61. Zima, A. V., E. Picht, …, L. A. Blatter. 2008. Termination of cardiac Ca2+ sparks: role of intra-SR [Ca2+], release flux, and intra-SR Ca2+ diffusion. *Circ. Res.* 103:e105–e115.

62. Brochet, D. X., W. Xie, …, W. J. Lederer. 2011. Quarky calcium release in the heart. *Circ. Res.* 108:210–218.

63. Matsuda, H., A. Noma, …, H. Irisawa. 1982. Transient depolarization and spontaneous voltage fluctuations in isolated single cells from guinea pig ventricles. Calcium-mediated membrane potential fluctuations. *Circ. Res.* 51:142–151.

64. Chen, W., G. Aistrup, …, Y. Shiferaw. 2011. A mathematical model of spontaneous calcium release in cardiac myocytes. *Am. J. Physiol. Heart Circ. Physiol.* 300:H1794–H1805.

65. Beuckelmann, D. J., M. Näbauer, and E. Erdmann. 1992. Intracellular calcium handling in isolated ventricular myocytes from patients with terminal heart failure. *Circulation.* 85:1046–1055.

66. Powell, T., M. F. Sturridge, …, V. W. Twist. 1981. Intact individual heart cells isolated from human ventricular tissue. *Br. Med. J. (Clin. Res.).* 283:1013–1015.

67. Satoh, H., L. M. Delbridge, …, D. M. Bers. 1996. Surface:volume relationship in cardiac myocytes studied with confocal microscopy and membrane capacitance measurements: species-dependence and developmental effects. *Biophys. J.* 70:1494–1504.

68. Jost, N., L. Virág, …, A. Varró. 2005. Restricting excessive cardiac action potential and QT prolongation: a vital role for IKs in human ventricular muscle. *Circulation.* 112:1392–1399.

69. Sakakibara, Y., T. Furukawa, …, J. A. Wasserstrom. 1993. Sodium current in isolated human ventricular myocytes. *Am. J. Physiol.* 265: H1301–H1309.

70. Mewes, T., and U. Ravens. 1994. L-type calcium currents of human myocytes from ventricle of non-failing and failing hearts and from atrium. *J. Mol. Cell. Cardiol.* 26:1307–1320.

71. Iost, N., L. Virág, …, J. G. Papp. 1998. Delayed rectifier potassium current in undiseased human ventricular myocytes. *Cardiovasc. Res.* 40:508–515.

72. Gerdes, A. M., S. E. Kellerman, …, D. D. Schocken. 1992. Structural remodeling of cardiac myocytes in patients with ischemic cardiomyopathy. *Circulation.* 86:426–430.

73. Shannon, T. R., F. Wang, …, D. M. Bers. 2004. A mathematical treatment of integrated Ca dynamics within the ventricular myocyte. *Biophys. J.* 87:3351–3371.

74. Pelzmann, B., P. Schaffer, …, B. Koidl. 1998. L-type calcium current in human ventricular myocytes at a physiological temperature from children with tetralogy of Fallot. *Cardiovasc. Res.* 38:424–432.

75. Magyar, J., N. Iost, …, P. P. Nanasi. 2000. Effects of endothelin-1 on calcium and potassium currents in undiseased human ventricular myocytes. *Pflugers Arch.* 441:144–149.

76. Fülöp, L., T. Bányász, …, P. P. Nánási. 2004. Reopening of L-type calcium channels in human ventricular myocytes during applied epicardial action potentials. *Acta Physiol. Scand.* 180:39–47.

77. Sun, L., J. S. Fan, …, P. T. Palade. 2000. A model of the L-type Ca2+ channel in rat ventricular myocytes: ion selectivity and inactivation mechanisms. *J. Physiol.* 529:139–158.

78. Zhang, J. F., P. T. Ellinor, …, R. W. Tsien. 1994. Molecular determinants of voltage-dependent inactivation in calcium channels. *Nature.* 372:97–100.

79. Matsuda, H. 1986. Sodium conductance in calcium channels of guinea-pig ventricular cells induced by removal of external calcium ions. *Pflugers Arch.* 407:465–475.

80. Yan, D. H., and K. Ishihara. 2005. Two Kir2.1 channel populations with different sensitivities to Mg(2+) and polyamine block: a model for the cardiac strong inward rectifier K(+) channel. *J. Physiol.* 563:725–744.

81. Ishihara, K., and D. H. Yan. 2007. Low-affinity spermine block mediating outward currents through Kir2.1 and Kir2.2 inward rectifier potassium channels. *J. Physiol.* 583:891–908.

82. Rajamani, S., L. L. Eckhardt, …, C. T. January. 2006. Drug-induced long QT syndrome: hERG K+ channel block and disruption of protein trafficking by fluoxetine and norfluoxetine. *Br. J. Pharmacol.* 149: 481–489.

83. Takeuchi, A., S. Tatsumi, …, A. Noma. 2006. Ionic mechanisms of cardiac cell swelling induced by blocking Na+/K+ pump as revealed by experiments and simulation. *J. Gen. Physiol.* 128:495–507.

84. Oka, C., C. Y. Cha, and A. Noma. 2010. Characterization of the cardiac Na+/K+ pump by development of a comprehensive and mechanistic model. *J. Theor. Biol.* 265:68–77.

85. Smith, N. P., and E. J. Crampin. 2004. Development of models of active ion transport for whole-cell modelling: cardiac sodium-potassium pump as a case study. *Prog. Biophys. Mol. Biol.* 85:387–405.

86. Tran, K., N. P. Smith, …, E. J. Crampin. 2009. A thermodynamic model of the cardiac sarcoplasmic/endoplasmic Ca(2+) (SERCA) pump. *Biophys. J.* 96:2029–2042.

87. Negroni, J. A., and E. C. Lascano. 1996. A cardiac muscle model relating sarcomere dynamics to calcium kinetics. *J. Mol. Cell. Cardiol.* 28:915–929.

88. Brochet, D. X., D. Yang, …, H. Cheng. 2005. Ca2+ blinks: rapid nanoscopic store calcium signaling. *Proc. Natl. Acad. Sci. USA.* 102:3099–3104.

89. Li, G. R., B. Yang, …, S. Nattel. 1999. Transmembrane ICa contributes to rate-dependent changes of action potentials in human ventricular myocytes. *Am. J. Physiol.* 276:H98–H106.

90. Pieske, B., B. Kretschmann, …, G. Hasenfuss. 1995. Alterations in intracellular calcium handling associated with the inverse force-frequency relation in human dilated cardiomyopathy. *Circulation.* 92:1169–1178.